

A hard molecular nanomagnet from confined paramagnetic 3d-4f spins inside a fullerene cage

Received: 26 July 2023

Accepted: 4 December 2023

Published online: 19 December 2023

Check for updates

Chenli Huang^{1,6}, Rong Sun^{2,6}, Lipiao Bao¹✉, Xinyue Tian¹, Changwang Pan¹, Mengyang Li³, Wangqiang Shen¹, Kun Guo¹, Bingwu Wang²✉, Xing Lu^{1,4}✉ & Song Gao^{2,5}

Reducing inter-spin distance can enhance magnetic interactions and allow for the realization of outstanding magnetic properties. However, achieving reduced distances is technically challenging. Here, we construct a 3d-4f metal cluster (Dy₂VN) inside a C₈₀ cage, affording a heretofore unseen metallofullerene containing both paramagnetic 3d and 4f metal ions. The significantly suppressed 3d-4f (Dy-V) distances, due to the unique cage confinement effect, were observed by crystallographic and theoretical analysis of Dy₂VN@I_h(7)-C₈₀. These reduced distances result in an enhanced magnetic coupling ($J_{\text{total, Dy-V}} = 53.30 \text{ cm}^{-1}$; $J_{\text{total, Dy-Dy}} = -6.25 \text{ cm}^{-1}$), leading to a high magnetic blocking temperature compared to reported 3d-4f single-molecule magnets and strong coercive field of 2.73 Tesla. Our work presents a new class of single-molecule magnets with both paramagnetic 3d and 4f metals confined in a fullerene cage, offering superior and tunable magnetic properties due to the unique cage confinement effect and the diverse composition of the entrapped magnetic core.

Magnets are omnipresent in daily life and play a prominent role in modern materials research and industry^{1–3}, spanning from magneto-mechanical machines to spintronics, high-density information storage and so on^{4–8}. Interactions between magnetic moment carriers are crucial to the construction of magnets⁹. The search for the origins and roles of magnetic interactions has shaped the development of not only magnets^{10–13} but also magnetic semiconductors^{14,15}, and even superconductors¹⁶.

Spin centers magnetically couple with each other in two ways, the dipolar interaction and the exchange interaction^{17,18}. The dipolar interaction arises from the influence of the magnetic field generated

by one of the spin centers on the other and is distance-dependent¹⁷, approximately inversely correlated to the cube of their distance. The essence of the exchange interaction is the overlap of magnetic orbitals or spin densities^{18,19}. Strong magnetic interactions are attractive due to the resulting magnetic properties. As a well-known example, strong interactions between the itinerant electrons in 3d transition metals and the 5d conduction band plus localized 4f electrons in lanthanides result in large magnetocrystalline anisotropies and high Curie temperature in rare earth-cobalt-based permanents, in particular making SmCo₅ the first commercial rare-earth permanent magnets^{10,11}.

¹State Key Laboratory of Materials Processing and Die & Mould Technology, School of Materials Science and Engineering, Huazhong University of Science and Technology, 1037, Luoyu Road, Wuhan 430074, P. R. China. ²Beijing National Laboratory of Molecular Science, State Key Laboratory of Rare Earth Materials Chemistry and Applications, College of Chemistry and Molecular Engineering, Peking University, Beijing 100871, P. R. China. ³School of Physics, Xidian University, Xi'an 710071, China. ⁴College of Chemistry and Chemical Engineering, Hainan University, No. 58, Renmin Avenue, Haikou 570228, P. R. China. ⁵Spin-X Institute, School of Chemistry and Chemical Engineering, State Key Laboratory of Luminescent Materials and Devices, Guangdong-Hong Kong-Macao Joint Laboratory of Optoelectronic and Magnetic Functional Materials, South China University of Technology, Guangzhou 510641, P. R. China. ⁶These authors contributed equally: Chenli Huang, Rong Sun. ✉e-mail: baol@hust.edu.cn; wangbw@pku.edu.cn; lux@hust.edu.cn

Unfortunately, obtaining strong magnetic interactions in molecular systems is challenging. The large ionic radius and shielding 4f orbits of lanthanide ions lead to weak 4f-4f interactions (usually smaller than 1 cm^{-1})^{20,21} and weak 3d-4f interactions (usually smaller than 10 cm^{-1})²²⁻²⁴. While shortening inter-spin distances could be an effective approach for enhancing magnetic coupling, metal spin centers in conventional coordination chemistry tend to be stabilized through definite coordination saturation, rendering effective distance reduction difficult due to the unavoidable solvent and ligand effects²⁵. Nevertheless, the above mentioned strong magnetic interactions in molecular systems play an important role, for an especially relevant example here, to help design high-performance single-molecule magnets (SMMs)—which may exhibit slow magnetic relaxation owing to their intrinsic anisotropy²⁶.

One promising and potentially straightforward approach for achieving strong magnetic interactions is to confine multiple magnetic metal centers within a fullerene cage thereby exploiting the unique coordination environment within the fullerene cage²⁷⁻³². The spatial confinement effect of fullerenes can effectively reduce the distances between spin centers and enhance the magnetic interaction. In addition, the shielding effect of the cages could also stabilize the internal clusters and make endohedral-metallofullerenes (EMFs) air-stable, essential for prospective applications. However, simultaneously introducing 3d and 4f spin centers into fullerene cages has never been reported due to the distinct synthetic difficulty.

Herein, we explored such class of metallofullerene containing both paramagnetic 4f and 3d metal elements, taking $\text{Dy}_2\text{VN}@I_h(7)\text{-C}_{80}$ as an example, whose molecular structure was unambiguously determined by X-ray crystallography. Due to the unique confinement effect of the fullerene cage on the endohedral Dy_2VN cluster, the distances

between the spin centers are significantly suppressed. The resulting enhanced magnetic interactions between confined spin centers ($J_{\text{total, Dy-V}} = 53.30\text{ cm}^{-1}$; $J_{\text{total, Dy-Dy}} = -6.25\text{ cm}^{-1}$) inhibit quantum tunneling of magnetization (QTM), which is the main factor hindering the performance of reported SMMs, and lead to a high blocking temperature (T_B) for 3d-4f SMMs and huge coercive field (H_c).

Results

Synthesis and crystal structure of $\text{Dy}_2\text{VN}@I_h(7)\text{-C}_{80}$

$\text{Dy}_2\text{VN}@I_h(7)\text{-C}_{80}$ was synthesized via a direct arc-discharge method and purified by high-performance liquid chromatographic (HPLC) separation. The analytical HPLC profile and high-resolution mass spectrum of $\text{Dy}_2\text{VN}@I_h(7)\text{-C}_{80}$ are shown in Fig. 1. The electronic properties of $\text{Dy}_2\text{VN}@I_h(7)\text{-C}_{80}$ were investigated by vis-NIR spectroscopic and cyclic voltametric (CV) studies. The absorption spectrum (Fig. 1c) of $\text{Dy}_2\text{VN}@I_h(7)\text{-C}_{80}$ displays four absorption peaks at 465, 581, 663, and 773 nm with the absorption onset at $\sim 1424\text{ nm}$, corresponding to an optical bandgap of 0.87 eV. These absorption bands have significant red shifts compared to those of the reported $\text{Dy}_2\text{ScN}@I_h(7)\text{-C}_{80}$ (absorption bands: 406, 565, 676, and 705 nm)³³, suggesting the crucial role of the entrapped V atom on the electronic structure of the whole EMF molecule. The recorded CV curves are shown in Fig. 1d and the characteristic redox potentials are listed in Table S4. $\text{Dy}_2\text{VN}@I_h(7)\text{-C}_{80}$ has one reversible oxidation process (0.05 V) and four reduction processes (-0.81, -1.53, -1.81, and -2.35 V), in which the first, third and fourth reduction processes are all reversible, but the second reduction process is irreversible. The first oxidation potential and the first reduction potential are 0.05 V and -0.81 V, respectively, resulting in an electrochemical bandgap of 0.86 eV, which is in perfect agreement with its optical bandgap.

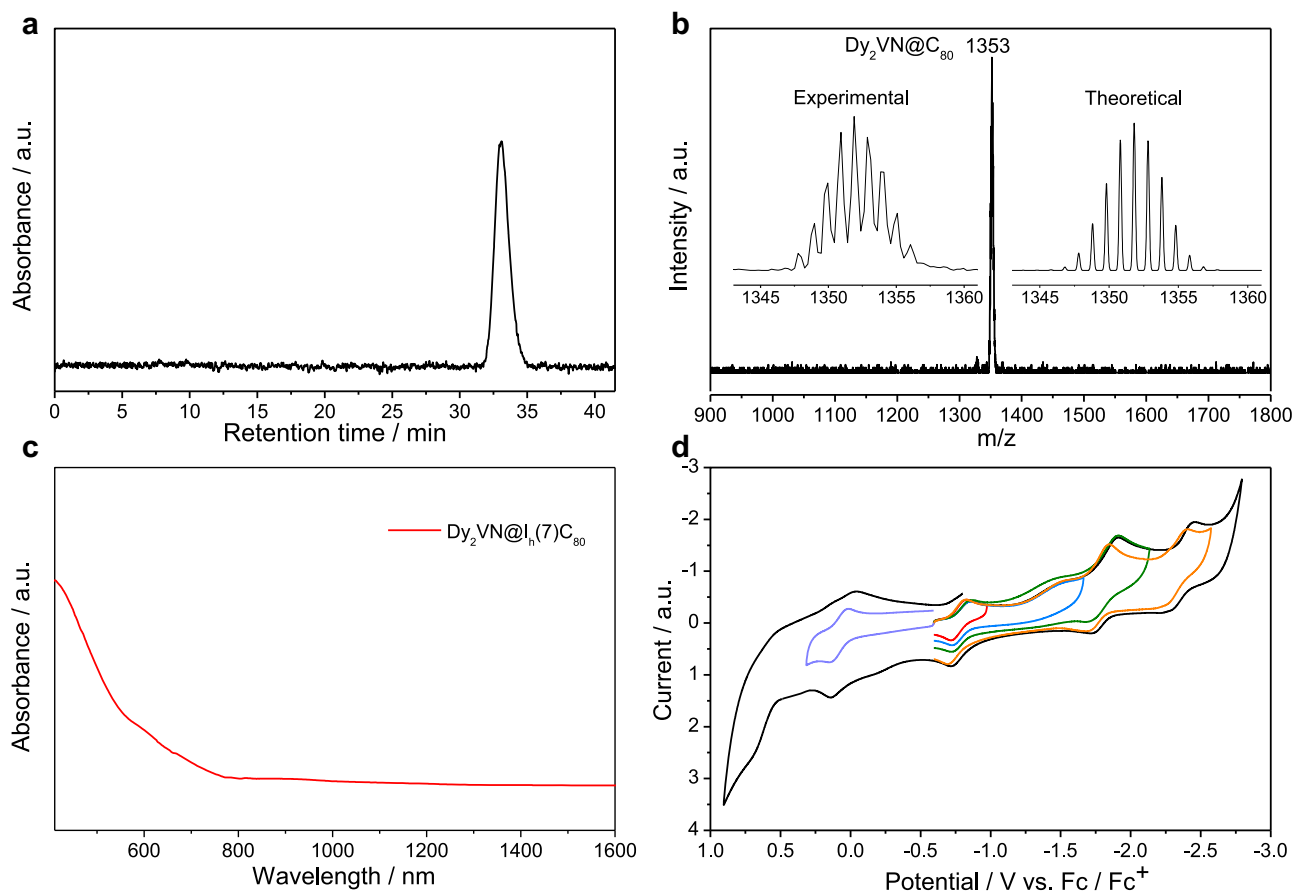


Fig. 1 | Characterizations of $\text{Dy}_2\text{VN}@I_h(7)\text{-C}_{80}$. **a** HPLC profile, **b** high-resolution mass spectrum, **c** absorption spectrum, and **d** CV curves of $\text{Dy}_2\text{VN}@I_h(7)\text{-C}_{80}$. Electrochemical conditions: 0.05 M tetrabutylammonium hexafluorophosphate (TBAPF₆) in *o*-dichlorobenzene (*o*-DCB) as electrolyte and 100 mV mL⁻¹ scan rate.

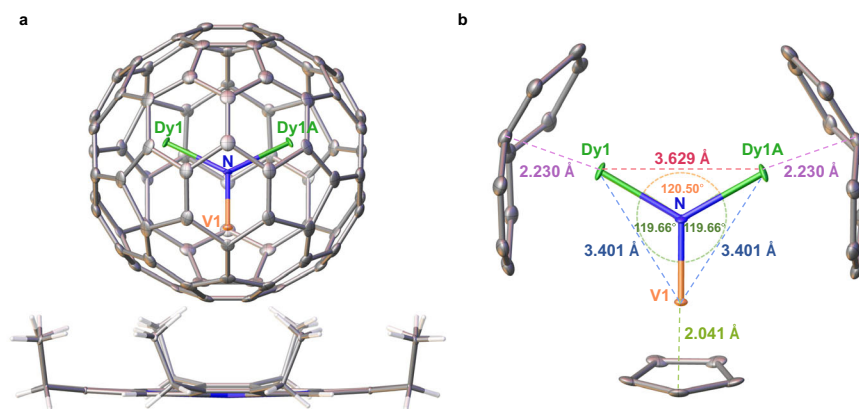


Fig. 2 | Crystal structure of $\text{Dy}_2\text{VN}@I_h(7)\text{-C}_{80}$. **a** Ortep drawing of $\text{Dy}_2\text{VN}@I_h(7)\text{-C}_{80}$ co-crystallized with $\text{Ni}(\text{OEP})$, where the thermal ellipsoids are set at 10% probability. Only one orientation of the fullerene cage together with the major site

of Dy_2VN cluster is shown and solvent molecules are omitted for clarity. **b** The positions of the major Dy_2VN site with respect to the nearest carbon atoms of the $I_h(7)\text{-C}_{80}$ cage. Green: Dy; Blue: N; Orange: V; Gray: C.

The molecular structure of $\text{Dy}_2\text{VN}@I_h(7)\text{-C}_{80}$ and interactions of the mixed metal atoms inside the cage are studied by X-ray crystallography (Fig. 2). Within the cage, the N atom is fully ordered, which locates on the crystallographic symmetric plane. Albeit of some disorder for Dy and V (Fig. S2 and Table S2), the major sites can be clearly distinguished. Dy1 with an occupancy value of 0.43 is the major Dy site and Dy1A generated by crystallographic operations from Dy1 is the other. The major V site locates on the crystallographic mirror plane with the occupancy value of 0.44. Due to the much smaller ion radius of V (0.64 Å) than that of Dy (0.91 Å), their metal-cage and metal-N distance show remarkable differences. The distance between Dy1 or Dy1A and the nearest cage carbon atom is 2.230 Å, whereas the distance between V1 and the nearest cage carbon atom is 2.041 Å. The relative orientation between the inner metals and the cage resembles that of $\text{Sc}_2\text{VN}@I_h(7)\text{-C}_{80}$ which also contains the transition metal V³⁺, but is obviously different from those of the reported lanthanide metal-based EMFs, such as $\text{MSc}_2\text{N}@I_h(7)\text{-C}_{80}$ (M=La, Ce, Gd, Tb)^{35–37} where the large lanthanide metal atom resides under the centers of hexagons while the small Sc atoms are close to an intersection between a hexagon and a pentagon. This dramatic difference demonstrates the crucial role of the entrapped transition metal V in the metal-cage interactions.

Within the Dy_2VN cluster, the bond length of Dy1-N is 2.090 Å while the V-N bond is significantly shorter (1.841 Å). These distinct differences allow us to unambiguously identify V from Dy, which is difficult to distinguish in other metallofullerenes containing mixed metals such as $\text{Sc}_{3-x}\text{V}_x\text{N}@C_{80}$ ($x=1-2$)^{34,38}. The included angles of Dy1-N-V1 and Dy1-N-Dy2 are 119.66° and 120.50°, respectively, so that the sum of the three angles is 359.82° ($\approx 360^\circ$), indicative of a planar structure of the Dy_2VN cluster. With the spatial confinement effect of the fullerene cage on the endohedral Dy_2VN cluster, the Dy-Dy distance has been significantly suppressed to 3.629 Å, which is the shortest among all the reported values for 3d-4f SMMs, as summarized in Table 1. The strong cage confinement is further reflected by the ultrashort Dy-V distance of 3.401 Å, which represents one of the smallest 3d-4f distances among all the reported 3d-4f SMMs. The compressed nature of the Dy_2VN cluster inside the cage is further verified by DFT calculations (Figure S7). The optimized geometry of $\text{Dy}_2\text{VN}@I_h(7)\text{-C}_{80}$ resembles the crystal structure and in particular confirms the ultrashort metal-metal distances. The calculated Dy-Dy and Dy-V distances are 3.631 Å and 3.491/3.331 Å, respectively, which are comparable to the recorded values in crystal structures (*vide supra*). Additional theoretical analysis shows weak Dy-Dy and Dy-V bonding with respective Wiberg bond order of 0.05 and 0.12/0.15, respectively. Such a unique cage confinement effect on the metals strengthens the interactions between the anisotropic lanthanide

metals, and enhances the 3d-4f magnetic coupling, slowing down the magnetic relaxation and improving the SMM performance (*vide infra*).

Magnetic properties

The magnetic properties of $\text{Dy}_2\text{VN}@I_h(7)\text{-C}_{80}$ were measured on a Quantum Design MPMS3 SQUID magnetometer (Fig. 3 and Fig. S3-S6). The temperature-dependent susceptibility data were collected under 1 kOe direct current (dc) field on the powder sample in the temperature range of 2–300 K. On cooling, the $\chi_m T$ values slightly go up from 26.4 cm³ K mol⁻¹ at 300 K to 27.02 cm³ K mol⁻¹ at 100 K and increase sharply with further cooling, reaching a maximum of 34.4 cm³ K mol⁻¹ at around 10 K (Fig. 3a). The significant increase of $\chi_m T$ values with temperature decreasing implies ferromagnetic interaction within the cluster. Below 10 K, the $\chi_m T$ values drop rapidly due to the depopulation of the Stark levels and magnetic anisotropies as the temperature decreases. The $\chi_m T$ value (26.4 cm³ K mol⁻¹) at 300 K is slightly smaller than the theoretical value of 29.34 cm³ K mol⁻¹ for two uncoupled Dy

Table 1 | Dy-Dy and 3d-4f distances in representative 3d-4f SMMs

3d-4f SMMs	Dy-Dy distance / Å	3d-4f distance / Å	ref.
$\text{Dy}_2\text{V}^{\text{III}}\text{N}$	3.629	3.401	<i>this work</i>
$\text{DyCu}^{\text{II}}_5$	N/A	3.904 ~ 3.964	39
$\text{Dy}_2\text{Cu}^{\text{II}}_{10}$	4.291	3.899 ~ 3.965	39
$\text{Dy}_2\text{Cr}^{\text{III}}_2$	4.105	3.290 ~ 3.302	40
$\text{Dy}_2\text{Fe}^{\text{III}}_4$	3.952	3.431 ~ 3.450 / 5.766 ~ 5.973	41
$\text{DyFe}^{\text{II}}_2$	N/A	3.520 ~ 3.599	22
$\text{Dy}_2\text{Co}^{\text{II}}_2$	6.183	3.489 ~ 3.496	23
$\text{Dy}_2\text{Mn}^{\text{II}}_2$	6.292	3.553 ~ 3.613	24
$\text{DyV}^{\text{IV}}\text{O}$	N/A	3.474	42
DyFe^{0}	N/A	2.88	43

$\text{Dy}_2\text{V}^{\text{III}}\text{N} = \text{Dy}_2\text{V}^{\text{III}}\text{N}@C_{80}$; $\text{DyCu}^{\text{II}}_5 = [\text{DyCu}^{\text{II}}_5(\text{quinha})_5(\text{sal})_2(\text{py})_5](\text{CF}_3\text{SO}_3)_2\text{py}\cdot 4\text{H}_2\text{O}$;³⁹
 $\text{Dy}_2\text{Cu}^{\text{II}}_{10} = [\text{Dy}_2\text{Cu}^{\text{II}}_{10}(\text{quinha})_{10}(\text{sal})_2(\text{OH})(\text{py})_5](\text{CF}_3\text{SO}_3)_3\cdot 2\text{py}\cdot 2\text{CH}_3\text{OH}\cdot 2\text{H}_2\text{O}$;³⁹
 $\text{Dy}_2\text{Cr}^{\text{III}}_2 = \text{Cr}^{\text{III}}_2\text{Dy}_2(\text{OME})_2(\text{O}_2\text{CPh})_4(\text{mdea})_2(\text{NO}_3)_2$;⁴⁰
 $\text{Dy}_2\text{Fe}^{\text{III}}_4 = [\text{Fe}^{\text{III}}_4\text{Dy}_2(\mu_3\text{-OH})_2(\text{mdea})_6(\text{SCN})_2(\text{NO}_3)_2(\text{H}_2\text{O})_2]\cdot 4\text{H}_2\text{O}\cdot 2\text{MeCN}$;⁴¹
 $\text{DyFe}^{\text{II}}_2 = [\text{Fe}^{\text{II}}_2\text{Dy}(\text{L})_2(\text{H}_2\text{O})_2]\text{ClO}_4\cdot 2\text{H}_2\text{O}$, L = 2,2',2''-(((nitritotris(ethane-2,1-diyl))tris(azanediyl))tris(methylene))tris(4-chlorophenol))²²
 $\text{Dy}_2\text{Co}^{\text{II}}_2 = [\text{Co}^{\text{II}}_2\text{Dy}_2(\text{L})_4(\text{NO}_3)_2(\text{THF})_2]\cdot 4\text{THF}$, $\text{H}_2\text{L} = (\text{E})\text{-}2\text{-}(2\text{-hydroxy-}3\text{-methoxybenzylideneamino})\text{phenol}$;²³
 $\text{Dy}_2\text{Mn}^{\text{II}}_2 = \text{Dy}_2\text{Mn}^{\text{II}}_2(\text{L})_4(\text{NO}_3)_2(\text{DMF})_2$, $\text{H}_2\text{L} = (\text{E})\text{-}2\text{-ethoxy-}6\text{-}((2\text{-hydroxyphenyl})\text{imino})\text{methylphenol}$;²⁴
 $\text{DyV}^{\text{IV}}\text{O} = \text{Dy}(\text{V}^{\text{IV}}\text{O})(\text{NO}_3)_3(\text{H}_2\text{O})$, $\text{H}_2\text{L} = \text{N}$, N'-bis(1-hydroxy-2-benzylidene-6-methoxy)-1,7-diamino-4-azaheptane;⁴²
 $\text{DyFe}^{\text{0}} = \text{PyCp}_2\text{Dy-FeCp}(\text{CO})_2$, $\text{PyCp}_2 = [\text{2,6-(CH}_2\text{C}_6\text{H}_5)_2\text{C}_5\text{H}_3\text{N}]^{2-}$, Cp = C_5H_5 ;⁴³

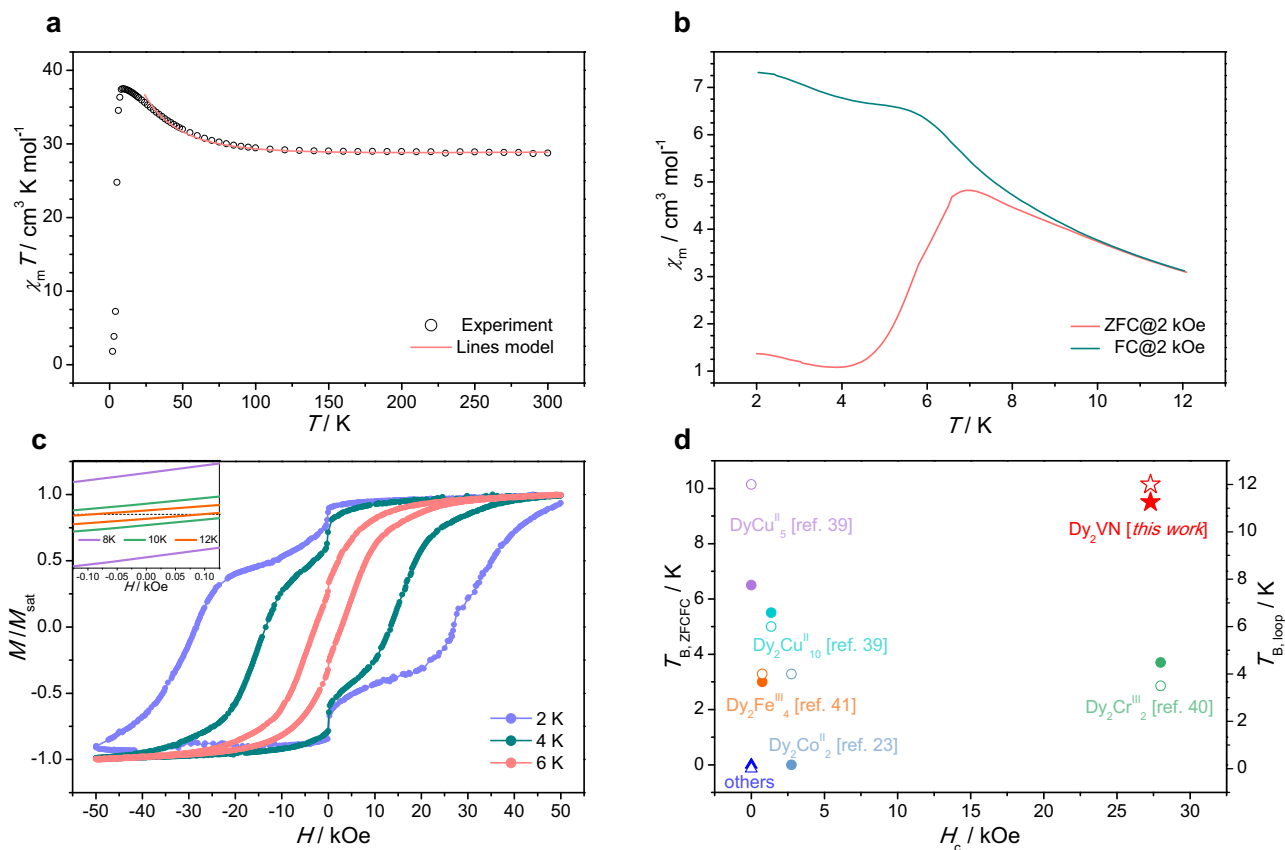


Fig. 3 | Magnetic properties of $\text{Dy}_2\text{VN}@I_h(7)\text{-C}_{80}$. **a** Temperature dependence of $\chi_m T$ products under 1 kOe dc field and the fitted temperature-dependent susceptibilities using Lines model. The experimental values were first scaled by a factor of 1.09 to make them consistent with the theoretical values at room temperature before fitting. **b** Zero-field-cooled (ZFC) magnetization and field-cooled (FC) magnetization under 2 kOe dc field at sweep rate of 3 K min^{-1} . **c** Magnetic hysteresis at different temperatures with the sweep rate of 200 Oe s^{-1} . The inset shows that the

opening hysteresis can be observed at up to 12 K. **d** Comparison of the blocking temperature ($T_{B, \text{ZFCFC}}$ and $T_{B, \text{loop}}$) and coercive field (H_c) between $\text{Dy}_2\text{VN}@I_h(7)\text{-C}_{80}$ and typical 3d-4f SMMs^{23,39–41}. The solid symbol represents $T_{B, \text{ZFCFC}}$ while the hollow symbol corresponds to $T_{B, \text{loop}}$. The pentacle represents $\text{Dy}_2\text{VN}@I_h(7)\text{-C}_{80}$ in this work. The triangle stands for the SMMs in Table S6 for which no related values are given. The circles stand for the other SMMs shown in Table S6.

(III) ions (the ground state ${}^6H_{15/2}$ and $g_J = 4/3$) and one V (III) ion ($S = 1$ and $g = 2$).

The zero-field-cooled (ZFC) magnetization and field-cooled (FC) magnetization (ZFC-FC) data were collected in the heating mode under 2 kOe dc field. The temperature of bifurcation in the ZFC-FC curve ($T_{B, \text{ZFCFC}}$) of $\text{Dy}_2\text{VN}@I_h(7)\text{-C}_{80}$ is determined to be 9.5 K (Fig. 3b), which offers the highest T_B in all reported 3d-4f SMMs (Fig. 3d and Table S6). In accordance with its $T_{B, \text{ZFCFC}}$, $\text{Dy}_2\text{VN}@I_h(7)\text{-C}_{80}$ exhibits open magnetic hysteresis up to 12 K ($T_{B, \text{loop}}$), as described in Fig. 3c. The hysteresis is quite broad with a coercive field of 2.73 T at 2 K (Fig. 3d and Fig. S5). To the best of our knowledge, this is among the largest coercive fields in all reported 3d-4f SMMs^{22–24,39–43} (Fig. 3d and Table S6).

Spin dynamics of $\text{Dy}_2\text{VN}@I_h(7)\text{-C}_{80}$ were also characterized by time-dependent dc measurements. Zero-field magnetization relaxation times τ below 15 K were determined by free-order exponential fitting of magnetization decay curves recorded after being magnetized by 1 kOe dc field (Fig. S6 and Table S7). The fitting of relaxation times τ vs. T^{-1} could be accomplished by combining Orbach and QTM processes using Eq. (1):

$$\tau^{-1} = \tau_0^{-1} \exp(-U_1/T) + \tau_{\text{QTM}}^{-1} \quad (1)$$

The best fit gives the Orbach barrier of $U_1 = 70.7 \text{ K}$ (Fig. 4a), which is actually the exchange barrier. And the fitted QTM relaxation time is $\tau_{\text{QTM}} = 1249.8 \text{ s}$ (Fig. 4a), indicating that QTM is effectively inhibited in

$\text{Dy}_2\text{VN}@I_h(7)\text{-C}_{80}$. T_B can also be obtained directly from the relaxation times. Sessoli et al. have suggested a more universal SMM characteristic, $T_{B, 100}$, the temperature at which the relaxation time is 100 s ⁴⁴. However, for most of the reported SMMs, the relaxation times were usually much shorter than 100 s within the detectable temperature range. To the best of our knowledge, there is only one 3d-4f SMM [$\text{Dy}_2\text{Cu}_{10}(\text{quinha})_{10}(\text{sal})_2(\text{OH})(\text{py})_9$]³⁺ whose $T_{B, 100}$ is ca. 2 K³⁹. For $\text{Dy}_2\text{VN}@I_h(7)\text{-C}_{80}$, $T_{B, 100}$ deduced from the temperature dependence of τ reaches to ca. 7.2 K.

Theoretical Analysis

The performance of polynuclear SMMs is affected not only by the magnetic anisotropy of single ion, but also the interactions between paramagnetic centers. Therefore, the exploration of magnetic interactions in polynuclear systems utilizing theoretical calculation is helpful to reveal the origin of magnetic relaxation. The studied molecule $\text{Dy}_2\text{VN}@I_h(7)\text{-C}_{80}$ is a three-center spin system and the magnetic states can be described with the total spin Hamiltonian (Eq. 2):

$$\hat{H}_{\text{tot}} = \hat{H}_{\text{CF}(\text{Dy}_1)} + \hat{H}_{\text{CF}(\text{Dy}_2)} + \hat{H}_{\text{ZFS}(\text{V})} - J_{\text{Dy,Dy}} \hat{J}_{\text{Dy}_1} \cdot \hat{J}_{\text{Dy}_2} - J_{\text{Dy,V}} (\hat{J}_{\text{Dy}_1} \cdot \hat{S}_V + \hat{J}_{\text{Dy}_2} \cdot \hat{S}_V) + \sum \hat{H}_{\text{Zeeman}} \quad (2)$$

where the first two terms describe the crystal-field (CF) effect of the Dy centers and the third stands for the zero-field splitting (ZFS) of the V center. The fourth and fifth terms describe the interactions between

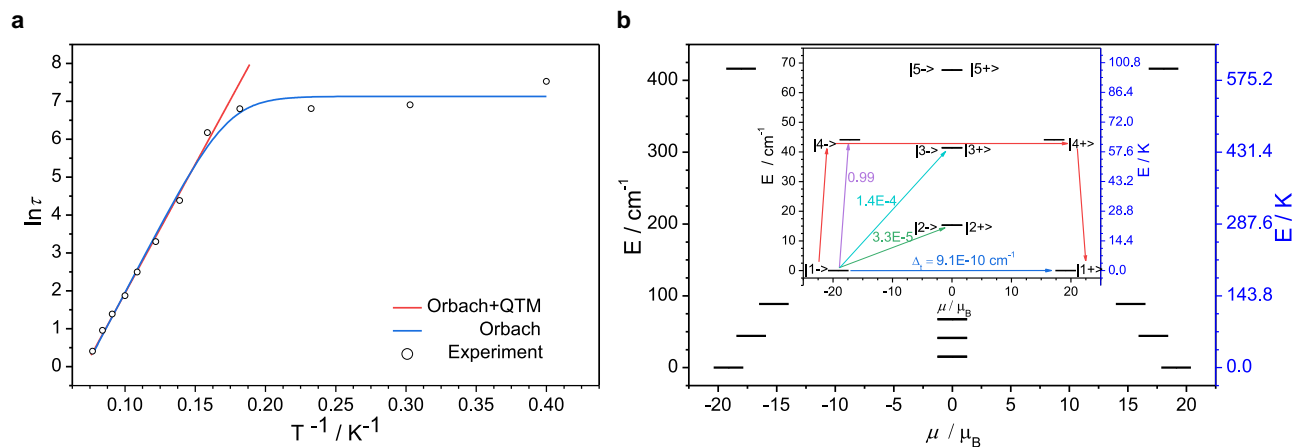


Fig. 4 | Exchange energy barriers of $\text{Dy}_2\text{VN}@I_h(7)\text{-C}_{80}$. **a** Plots of the logarithm of the relaxation times ($\ln \tau$) vs. reciprocal temperature (T^{-1}). The circles represent the relaxation times τ extracted from magnetization decay curves. The blue solid line indicates the fitting with the combination of Orbach and QTM processes, while the red line represents the result of only using Orbach process above 6 K (see in Supporting Information). **b** Energy levels obtained from Lines model. The black lines

represent the pseudo-doublets as a function of their magnetic moments along the magnetic axis. Inset: low-lying energy levels of the exchange part. The number at each arrow stands for the mean absolute value of the corresponding matrix element of the transition magnetic moment. The red arrow corresponds to the deduced relaxation pathway ($U_{\text{Lines}} = 63.4 \text{ K}$).

the magnetic centers while the last term represents the Zeeman interaction. The interactions between different Dy centers and V center are considered to be identical as the two Dy centers are structurally identical.

Before proceeding to the discussion of the interactions within the cluster and understanding the energy-level spectrum simulated with the Hamiltonian (Eq. 2), single-ion CF parameters for Dy center and ZFS parameters for V center need to be treated properly. Ab initio calculations were performed at the CASSCF/SO-RASSI level of theory⁴⁵. The computational results show that both Dy centers have strong uniaxial magnetic anisotropy and the ground state easy-axis is aligned along the metal-nitrogen bond, as shown in Fig. S8. The calculated ground state g tensors of Dy centers are very close to the values of the Ising limit states and the overall crystal-field splitting is up to 1500 cm^{-1} , with the first excited state of higher than 400 cm^{-1} (Table S10). In contrast, the calculated E/D for V center is 0.31, thus it could be treated as isotropic with an average g_{iso} of 1.9. The calculated high magnetic excited states of both single Dy center and V center indicate that the much lower U_1 may stem from the magnetic coupling of spin centers within the fullerene cage.

With the corresponding magnetic properties of the mononuclear fragments in hand, the magnetic interactions were explored to further elucidate the magnetic relaxation of $\text{Dy}_2\text{VN}@I_h(7)\text{-C}_{80}$. The temperature-dependent susceptibilities of $\text{Dy}_2\text{VN}@I_h(7)\text{-C}_{80}$ were fitted based on Eq. (2) and only the data above 20 K were considered during the fitting (See in Methods, Fig. 3a). Given the fitting result from Table 2, the interaction between Dy centers is characterized as anti-ferromagnetic while the interaction between Dy and V is ferromagnetic. The exchange-coupled levels and g -tensor values of $\text{Dy}_2\text{VN}@I_h(7)\text{-C}_{80}$ were also calculated and summarized in Table S11. These levels are grouped into pseudo-doublets split by the tunneling gap (Δ_t) because of the even number of unpaired electrons in

$\text{Dy}_2\text{VN}@I_h(7)\text{-C}_{80}$. The calculated ground exchange state features an extremely small Δ_t , indicating that QTM is suppressed and large H_c could be observed. On the contrast, the third excited pseudo-doublet possesses a relatively large Δ_t , thus the relaxation pathway could be deduced as indicated with red arrows in Fig. 4b combining with the transition probabilities. The inferred exchange barrier gives $U_{\text{Lines}} = 63.4 \text{ K}$ and is well consistent with the energy barrier fitted from the data of demagnetization ($U_1 = 70.7 \text{ K}$). Although the splitting of the energy states is much lower than the crystal-field splitting of an individual Dy(III), the strong coupling between Dy(III) and V(III) can effectively suppress QTM, leading to large coercivity and high T_B .

Discussion

Enhancing magnetic coupling of paramagnetic centers is an effective strategy for realizing excellent SMM behaviors. Strong interactions between the metal centers in $\text{Dy}_2\text{VN}@I_h(7)\text{-C}_{80}$ bring about negligible transverse components of g -tensor ($g_x = g_y = 0$) and large magnetic moment of the ground state, which suppress QTM and lead to hard magnetism. In 2014, Greber et al.⁴⁶ reported the magnetic properties of $\text{Dy}_n\text{Sc}_{3-n}\text{N}@I_h\text{-C}_{80}$ ($n = 1, 2, 3$) containing different numbers of paramagnetic Dy(III). The different hysteresis behaviors of $\text{Dy}_n\text{Sc}_{3-n}\text{N}@I_h\text{-C}_{80}$ ($n = 1, 2, 3$) revealed that the number of magnetic metal ions and their interactions have a significant influence on the properties of EMFs. In zero field, the magnetization of $\text{DySc}_2\text{N}@I_h\text{-C}_{80}$ decays rapidly via quantum tunneling. For $\text{Dy}_2\text{ScN}@I_h\text{-C}_{80}$, the demagnetization needs to overcome the exchange barrier or simultaneously reverse the magnetic moments of the two Dy(III) ions, which suppresses QTM and cause remanence. The much narrower hysteresis of $\text{Dy}_2\text{ScN}@I_h\text{-C}_{80}$ in comparison to $\text{Dy}_2\text{VN}@I_h(7)\text{-C}_{80}$ also demonstrates that the strong coupling (53.3 cm^{-1}) between Dy(III) and paramagnetic V(III) is fundamental for magnetic relaxation, while in $\text{Dy}_2\text{ScN}@I_h\text{-C}_{80}$ there is only a much weaker Dy-Dy interaction. The introduction of paramagnetic V(III) instead of diamagnetic Sc(III) could result in multilevel exchange states and suppress QTM, leading to larger H_c (0.5 T at 2 K with sweep rate at 80 Oe s^{-1} for $\text{Dy}_2\text{ScN}@I_h\text{-C}_{80}$). The noncolinear ferromagnetic coupling among both paramagnetic centers in $\text{Dy}_3\text{N}@I_h\text{-C}_{80}$ leads to a frustrated ground state, where the tunneling between six-fold degenerate ground states may facilitate demagnetization and cause much weaker remanence than in $\text{Dy}_2\text{ScN}@I_h\text{-C}_{80}$. In contrast, replacing one Dy(III) with a V(III), the six-fold degeneration in $\text{Dy}_3\text{N}@I_h\text{-C}_{80}$ was broken. Combining with the strong interaction

Table 2 | The magnetic interactions obtained using Lines model

	Dy-Dy	Dy-V
$J_{\text{dip}} / \text{cm}^{-1}$	6.25	0.80
$J_{\text{exch}} / \text{cm}^{-1}$	-12.5	52.50
$J_{\text{total}} / \text{cm}^{-1}$	-6.25	53.30

between 3d-4f metals, the broken degeneracy could effectively inhibit QTM, making $\text{Dy}_2\text{VN}@I_h(7)\text{-C}_{80}$ one of the most remarkable SMMs.

The presence of metal bonds can effectively enhance magnetic coupling, and the three-spin $[\text{Ln}^{3+}\text{-e-Ln}^{3+}]$ systems^{28–30} with strong coupling have shown promise as SMMs. Nevertheless, the larger magnetic moment of V(III) resulted in larger remanence of $\text{Dy}_2\text{VN}@I_h(7)\text{-C}_{80}$ than $\text{Dy}_2\text{V}@C_{80}(\text{CH}_2\text{Ph})$ (1.15 T at 2 K with sweep rate at 29 Oe s^{-1}) and $\text{Dy}_2\text{V}@C_{79}\text{N}$ (1.5 T at 2 K with sweep rate at 200 Oe s^{-1}). In that way, paramagnetic 3d metals are of vital importance to 3d-4f SMM behavior and a diverse array of 3d-4f SMMs have been reported (Table S6). Generally speaking, the enhanced magnetic coupling between paramagnetic lanthanides and 3d ions can be an effective means to improve the performance of SMMs, while the unique confinement effect of fullerenes may compress the distance between spin centers and enhance coupling.

In summary, a metal cluster Dy_2VN has been confined inside a C_{80} fullerene cage, forming a metallofullerene containing both paramagnetic 4f and 3d metal ions. The molecular structure and internal metal interactions of $\text{Dy}_2\text{VN}@I_h(7)\text{-C}_{80}$ were systematically studied by X-ray crystallography. The unique confinement effect of the cage leads to strong internal Dy-Dy and Dy-V interactions, as reflected by the ultrashort Dy-Dy and Dy-V distances. As a result of the strong magnetic coupling inside the cage, $\text{Dy}_2\text{VN}@I_h(7)\text{-C}_{80}$ shows a record-high blocking temperature among all reported 3d-4f SMMs and huge coercive field. Our work opens a new class of 3d-4f SMMs based on EMFs, with superior magnetic properties endowed by the unique confinement effect of the cage. The construction of this new class of 3d-4f SMMs can be achieved through a modular approach by concurrent metal encapsulation inside the fullerene cage. Considering the diversity of the cage geometry, cluster structure and exohedral chemical functionalization on the cage, the range of possibilities for the magnetic properties of such SMMs is extensive.

Methods

Synthesis

Dy_2O_3 and vanadium carbide were used as metal sources to synthesize the mixed nitride cluster fullerenes with embedded Dy and V metals. Raw soot of EMFs was obtained by an arc-discharge method. The soot was extracted with CS_2 . After the removal of CS_2 , the residue was re-dissolved in toluene and the solution was subjected to multi-stage high-performance liquid chromatographic (HPLC) separation. Details of the separation process are described in the Supporting Information (Fig. S1).

X-ray crystallography

Single crystals of $\text{Dy}_2\text{VN}@I_h(7)\text{-C}_{80}$ were obtained by layering a benzene solution of Ni (OEP) (OEP is the dianion of octaethylporphyrin) atop of a saturated CS_2 solution of $\text{Dy}_2\text{VN}@I_h(7)\text{-C}_{80}$ in a glass tube. After two weeks, the two solutions diffused together and black crystals formed. X-ray data were collected at 100 K using a radiation wavelength of 0.67012 Å at beamline BL17B of the Shanghai Synchrotron Radiation Facility. A multi-scan method was used for absorption corrections. The structures were solved with direct methods and were refined with SHELXL-2018. CCDC 2193585 contains the supplementary crystallographic data of this paper. Details of the structural refinement can be found in the Supporting Information.

Magnetometry

Magnetic properties were determined using a Quantum Design MPMS3 magnetometer. DC mode was adopted for the measurements of susceptibility and magnetization, while VSM mode was selected for hysteresis, zero-field-cooled (ZFC) magnetization and field-cooled (FC) magnetization (ZFC-FC) and magnetization decay measurements. The sample (0.340 mg) was prepared by drop-casting from carbon

disulfide solution onto a slice of Al foil (5.413 mg) which is paramagnetic to minimize the background of sample holder. Then, fast evaporation of carbon disulfide afforded black powder. After that, the Al foil was folded into a small cube and stuck on the inner wall of a plastic straw with a tiny amount of N grease (less than 1 mg). The background of Al foil and Pascal correction were considered when the point-by-point correction was carried on the data.

Theoretical calculations

Ab initio calculations of the $\text{Dy}_2\text{VN}@I_h(7)\text{-C}_{80}$ model systems have been performed at the CASSCF/SO-RASSI level of theory employing the quantum chemistry package MOLCAS 8.1⁴⁷. Dynamic correlation energy was considered using the CASPT2 program for the calculation of V(III). The single-ion magnetic properties and CF/ZFS parameters were calculated with SINGLE_ANISO program^{45,48,49} based on the ab initio results. The calculation models were built on the basis of crystal structure and without further optimization. For the calculation of electronic structure of a single Dy center, the other Dy(III) was replaced by a diamagnetic Lu(III) while V(III) was replaced with a diamagnetic Sc(III) in the model molecule. Similarly, both Dy centers were replaced with Lu(III) in the magnetic calculation of V(III). The magnetic states of $\text{Dy}_2\text{VN}@I_h(7)\text{-C}_{80}$ can be described with the total spin Hamiltonian (Eq. 2), where $J_{\text{Dy,Dy}}$ represents total interactions (including dipolar and exchange interaction) between Dy centers and \hat{J}_{Dy} is the localized dysprosium magnetic moment. Similarly, $J_{\text{Dy,V}}$ represents total interactions between Dy and V, and \hat{S}_V is the spin of V(III). With the corresponding magnetic properties of the mononuclear fragments in hand, the magnetic interactions were then explored. The anisotropic exchange interactions between the magnetic centers were considered within the Lines model⁵⁰ using the Hamiltonian (Eq. 3):

$$\hat{H}_{\text{exchange}} = -J_{\text{exch,DyDy}}\tilde{S}_{\text{Dy}1,z} \cdot \tilde{S}_{\text{Dy}2,z} - J_{\text{exch,DyV}}(\tilde{S}_{\text{Dy}1,z} \cdot \hat{S}_V + \tilde{S}_{\text{Dy}2,z} \cdot \hat{S}_V) \quad (3)$$

while the dipole-dipole magnetic coupling is treated exactly (see details in Supporting Information). The first term describes the exchange interaction between the two Dy centers and the second one corresponds to the exchange interaction between Dy and V center. The subscript of the pseudospin/spin operators denotes the local anisotropy axis on the corresponding metal center. The spin of V(III) was regarded as $S = 1$, while Dy(III) was treated with the pseudospin $\tilde{S} = 1/2$. The temperature-dependent susceptibilities of $\text{Dy}_2\text{VN}@I_h(7)\text{-C}_{80}$ were fitted employing the POLY_ANISO program^{48,49}.

Data availability

All data supporting the findings of this study are available with the paper and its supplementary information files. The crystallographic data for $\text{Dy}_2\text{VN}@I_h(7)\text{-C}_{80}$ in this study have been deposited at the Cambridge Crystallographic Data Centre under CCDC number 2193585 [<https://doi.org/10.5517/ccdc.csd.cc2cmltf>]. The data are also available from the corresponding authors upon reasonable request.

References

- White, R. M. Opportunities in magnetic materials. *Science* **229**, 11–15 (1985).
- Robinson, A. L. Powerful new magnet material found. *Science* **223**, 920–922 (1984).
- Tilley, D. R. Magnets. *Nature* **228**, 957 (1984).
- Laakso, S. V. A. et al. Dull punch line is not a joke - Worn cutting edge causes higher iron losses in electrical steel piercing. *Robot. Comput. Integr. Manuf.* **55**, 141–146 (2019).
- Bogani, L. & Wernsdorfer, W. Molecular spintronics using single-molecule magnets. *Nat. Mater.* **7**, 179–186 (2008).

6. Wernsdorfer, W. & Sessoli, R. Quantum phase interference and parity effects in magnetic molecular clusters. *Science* **284**, 133–135 (1999).
7. Leuenberger, M. N. & Loss, D. Quantum computing in molecular magnets. *Nature* **410**, 789–793 (2001).
8. Watkins, N. D. Magnetic telechemistry is elegant but nature is complex. *Nature* **251**, 497–498 (1974).
9. Miller, J. S. & Epstein, A. J. Organic and organometallic molecular magnetic materials-designer magnets. *Angew. Chem. Int. Ed. Engl.* **33**, 385–415 (1994).
10. Strnat, K. et al. A family of new cobalt-base permanent magnet materials. *J. Appl. Phys.* **38**, 1001–1002 (1967).
11. Strnat, K. J. & Strnat, R. M. W. Rare earth-cobalt permanent magnets. *J. Magn. Magn. Mater.* **100**, 38–56 (1991).
12. Zeng, H. et al. Exchange-coupled nanocomposite magnets by nanoparticle self-assembly. *Nature* **420**, 395–398 (2002).
13. Gould, C. A. et al. Ultrahard magnetism from mixed-valence dlanthanide complexes with metal-metal bonding. *Science* **375**, 198–202 (2022).
14. Zeng, Y. et al. 2D FeOCl: A highly in-plane anisotropic anti-ferromagnetic semiconductor synthesized via temperature-oscillation chemical vapor transport. *Adv. Mater.* **34**, 2108847 (2022).
15. Bae, Y. J. et al. Exciton-coupled coherent magnons in a 2D semiconductor. *Nature* **609**, 282–286 (2022).
16. Persky, E. et al. Magnetic memory and spontaneous vortices in a van der Waals superconductor. *Nature* **607**, 692–696 (2022).
17. Kahn, O. *Molecular Magnetism*. (VCH, 1993).
18. R. Boca. *Theoretical Foundations of Molecular Magnetism*. (Elsevier Science S. A., 1999).
19. Coronado, E. et al. In *Molecular Magnetism: From Molecular Assemblies to the Devices*, (Kluwer, 1996).
20. Long, J. et al. Single-molecule magnet behavior for an anti-ferromagnetically superexchange-coupled dinuclear dysprosium(III) complex. *J. Am. Chem. Soc.* **133**, 5319–5328 (2011).
21. Le Roy, J. J. et al. Coupling strategies to enhance single-molecule magnet properties of erbium-cyclooctatetraenyl complexes. *J. Am. Chem. Soc.* **136**, 8003–8010 (2014).
22. Liu, J.-L. et al. A heterometallic Fe^{II}-Dy^{III} single-molecule magnet with a record anisotropy barrier. *Angew. Chem. Int. Ed.* **53**, 12966–12970 (2014).
23. Mondal, K. C. et al. Coexistence of distinct single-ion and exchange-based mechanisms for blocking of magnetization in a Co^{II}-Dy^{III}₂ single-molecule magnet. *Angew. Chem. Int. Ed.* **51**, 7550–7554 (2012).
24. Li, J. et al. Tuning quantum tunnelling of magnetization through 3d–4f magnetic interactions: an alternative approach for manipulating single-molecule magnetism. *Inorg. Chem. Front.* **4**, 114–122 (2017).
25. Beillard, A. et al. Alternative technologies that facilitate access to discrete metal complexes. *Chem. Rev.* **119**, 7529–7609 (2019).
26. Sessoli, R. et al. Magnetic bistability in a metal-ion cluster. *Nature* **365**, 141–143 (1993).
27. Chen, C.-H. et al. Magnetic hysteresis in self-assembled monolayers of Dy-fullerene single molecule magnets on gold. *Nanoscale* **10**, 11287–11292 (2018).
28. Liu, F. et al. Single molecule magnet with an unpaired electron trapped between two lanthanide ions inside a fullerene. *Nat. Commun.* **8**, 16098 (2017).
29. Wang, Y. et al. Dy₂@C₇₉N: a new member of dimetalloazafullerenes with strong single molecular magnetism. *Nanoscale* **12**, 11130–11135 (2020).
30. Velkos, G. et al. High blocking temperature of magnetization and giant coercivity in the azafullerene Tb₂@C₇₉N with a single-electron terbium-terbium bond. *Angew. Chem. Int. Ed.* **58**, 5891–5896 (2019).
31. Nie, M. et al. A luminescent single-molecule magnet of dimetallofullerene with cage-dependent properties. *Nanoscale* **11**, 18612–18618 (2019).
32. Liu, F. et al. Mononuclear Clusterfullerene Single-Molecule Magnet Containing Strained Fused-Pentagons Stabilized by a Nearly Linear Metal Cyanide Cluster. *Angew. Chem. Int. Ed.* **129**, 1856–1860 (2017).
33. Yang, S. et al. Mixed metal nitride clusterfullerenes in cage isomers: Lu_xSc_{3-x}N@C₈₀(x = 1, 2) as compared with M_xSc_{3-x}N@C₈₀(M = Er, Dy, Gd, Nd). *J. Phys. Chem. C.* **113**, 7616–7623 (2009).
34. Wei, T. et al. Entrapping a group-VB transition metal, vanadium, within an endohedral metallofullerene: V_xSc_{3-x}N@I_hC₈₀ (x = 1, 2). *J. Am. Chem. Soc.* **138**, 207–214 (2016).
35. Stevenson, S. et al. Internal and external factors in the structural organization in cocrystals of the mixed-metal endohedrals (GdSc₂N@I_h-C₈₀, Gd₂ScN@I_h-C₈₀, and TbSc₂N@I_h-C₈₀) and Nickel(II) octaethylporphyrin. *Inorg. Chem.* **47**, 1420–1427 (2008).
36. Stevenson, S. et al. Selective synthesis, isolation, and crystallographic characterization of LaSc₂N@I_h-C₈₀. *Inorg. Chem.* **51**, 13096–13102 (2012).
37. Wang, X. et al. Preparation and structure of CeSc₂N@C₈₀: an icosahedral carbon cage enclosing an acentric CeSc₂N unit with buried f electron spin. *J. Am. Chem. Soc.* **128**, 8884–8889 (2006).
38. Wei, T. et al. Blending non-Group-3 transition metal and rare-earth metal into a C₈₀ fullerene cage with D_{5h} symmetry. *Angew. Chem. Int. Ed.* **57**, 10273–10277 (2018).
39. Wang, J. et al. Opening magnetic hysteresis by axial ferromagnetic coupling: from mono-decker to double-decker metallacrown. *Angew. Chem. Int. Ed.* **60**, 5299–5306 (2021).
40. Langley, S. K. et al. A {Cr^{III}₂Dy^{III}₂} single-molecule magnet: enhancing the blocking temperature through 3d magnetic exchange. *Angew. Chem. Int. Ed.* **52**, 12014–12019 (2013).
41. Akhtar, M. N. et al. Exploring the role of intramolecular interactions in the suppression of quantum tunneling of the magnetization in a 3d-4f single-molecule magnet. *Inorg. Chem.* **60**, 9302–9308 (2021).
42. Kotrlé, K. et al. 3d–4f magnetic exchange interactions and anisotropy in a series of heterobimetallic vanadium(IV)-lanthanide(III) Schiff base complexes. *Dalton Trans.* **50**, 13883–13893 (2021).
43. Burns, C. P. et al. Structure and Magnetization Dynamics of Dy–Fe and Dy–Ru Bonded Complexes. *Angew. Chem. Int. Ed.* **57**, 8144–8148 (2018).
44. Gatteschi, D., Sessoli, R. & Villain, J. *Molecular Nanomagnets*. (Oxford University Press, 2006).
45. Chibotaru, L. F. & Ungur, L. Ab initio calculation of anisotropic magnetic properties of complexes. I. Unique definition of pseudospin Hamiltonians and their derivation. *J. Chem. Phys.* **137**, 064112 (2012).
46. Westerström, R. et al. Tunneling, remanence, and frustration in dysprosium-based endohedral single-molecule magnets. *Phys. Rev. B* **89**, 060406 (2014).
47. Aquilante, F. et al. Molcas 8: New capabilities for multi-configurational quantum chemical calculations across the periodic table. *J. Comput. Chem.* **37**, 506–541 (2016).
48. Chibotaru, L. F. et al. Structure, magnetism, and theoretical study of a mixed-valence Coll3Coll4 heptanuclear wheel: lack of SMM behavior despite negative magnetic anisotropy. *J. Am. Chem. Soc.* **130**, 12445–12455 (2008).
49. Chibotaru, L. F., Ungur, L. & Soncini, A. The origin of nonmagnetic Kramers doublets in the ground State of dysprosium triangles: evidence for a toroidal magnetic moment. *Angew. Chem. Int. Ed.* **47**, 4126–4129 (2008).
50. Lines, M. E. Orbital angular momentum in the theory of paramagnetic clusters. *J. Chem. Phys.* **55**, 2977–2984 (1971).

Acknowledgements

L.B. acknowledges the support from NSFC (No. 22201086). X.L. acknowledges financial support from NSFC (Nos. 21925104, 92261204)

and the Hubei Provincial Natural Science Foundation of China (No. 2021CFA020). B.W. acknowledges the support by the NSFC (Nos. 21971006, 22131003) and the National Basic Research Program of China (No. 2018YFA0306003). C.P. acknowledges the support from NSFC (No. 21901090). W.S. acknowledges the support from NSFC (No. 22001084). We thank the staff in BL17B beamline of National Center for Protein Sciences Shanghai (NCPSS) at Shanghai Synchrotron Radiation Facility for the assistance with data collection, and the Analytical and Testing Center in Huazhong University of Science and Technology for all related measurements. All the calculations were supported by the High-performance Computing Platform of Peking University and Hefei Advanced Computing Center.

Author contributions

L.B., B.W., and X.L. conceived the research and co-supervised the project. C.H. and X.T. synthesized, isolated, and purified the product and performed all structural characterizations with assistance from W.S., and K.G. R.S. carried out magnetic characterization, theoretical calculations, and analyzed the data. C.P. and L.B. performed the crystallographic analysis. M.L. performed the DFT calculations. C.H., R.S., and L.B. co-wrote the manuscript. S.G. participated in discussions and gave out valuable comments on this manuscript. All authors discussed the results and contributed to writing the manuscript.

Competing interests

The authors declare no competing interests.

Additional information

Supplementary information The online version contains supplementary material available at <https://doi.org/10.1038/s41467-023-44194-y>.

Correspondence and requests for materials should be addressed to Lipiao Bao, Bingwu Wang or Xing Lu.

Peer review information *Nature Communications* thanks the anonymous reviewers for their contribution to the peer review of this work. A peer review file is available.

Reprints and permissions information is available at <http://www.nature.com/reprints>

Publisher's note Springer Nature remains neutral with regard to jurisdictional claims in published maps and institutional affiliations.

Open Access This article is licensed under a Creative Commons Attribution 4.0 International License, which permits use, sharing, adaptation, distribution and reproduction in any medium or format, as long as you give appropriate credit to the original author(s) and the source, provide a link to the Creative Commons licence, and indicate if changes were made. The images or other third party material in this article are included in the article's Creative Commons licence, unless indicated otherwise in a credit line to the material. If material is not included in the article's Creative Commons licence and your intended use is not permitted by statutory regulation or exceeds the permitted use, you will need to obtain permission directly from the copyright holder. To view a copy of this licence, visit <http://creativecommons.org/licenses/by/4.0/>.

© The Author(s) 2023